1-1-2017

Detection of diffuse seafloor venting using a structured light laser sensor: 1. Development of a classification based detection method

Clara Smart
University of Rhode Island

Chris Roman
University of Rhode Island

Steven Carey
University of Rhode Island

Citation/Publisher Attribution

Smart, Clara, Chris Roman, and Steven Carey. "Detection of diffuse seafloor venting using a structured light laser sensor: 1. Development of a classification based detection method." *Earth and Space Science* 4, 6 (2017): 348-363. doi: 10.1002/2017EA000262.

Detection of diffuse seafloor venting using a structured light laser sensor: 1. Development of a classification based detection method

Keywords

hydrothermal vent detection; hydrothermal venting; machine learning; seafloor mapping; structured light laser sensor

AGU PUBLICATIONS

Earth and Space Science

RESEARCH ARTICLE
10.1002/2017EA000262

This article is a companion to *Smart and Roman* [2017], doi:10.1002/2017EA000263.

Key Points:
- The vehicle-mounted structured light laser sensor is sensitive to turbulent density anomalies
- Detection algorithm advancements include normalization and the machine classification routines
- Resulting maps of multiple vent field sites successfully classify seafloor, bacteria, and active venting

Correspondence to:
C. Smart,
csmart@my.uri.edu

Citation:
Smart, C., C. Roman, and S. Carey (2017), Detection of diffuse seafloor venting using a structured light laser sensor: 1. Development of a classification based detection method, *Earth and Space Science*, *4*, 348–363, doi:10.1002/2017EA000262.

Received 7 FEB 2017
Accepted 17 MAY 2017
Accepted article online 6 JUN 2017
Published online 28 JUN 2017

Detection of diffuse seafloor venting using a structured light laser sensor: 1. Development of a classification based detection method

Clara Smart[1], Chris Roman[1,2], and Steven Carey[2]

[1]Department of Ocean Engineering, University of Rhode Island, Narragansett, Rhode Island, USA, [2]Graduate School of Oceanography, University of Rhode Island, Narragansett, Rhode Island, USA

Abstract Systematic and remote detection of diffuse hydrothermal venting is complex yet necessary to establish a comprehensive understanding the distribution, contribution, and context of fluid flow within hydrothermal systems. Diffuse flow is characterized by both low temperature and low flow rates and cannot be consistently distinguished during extensive systematic surveys using current vehicle-mounted visual, acoustic, or environmental sensors. The remotely operated vehicle-mounted structured light laser sensor is sensitive to fluid density anomalies and seafloor characteristics. Presented advancements to the detection algorithm include the development and implementation of intensity normalization routines and a support vector machine classification algorithm. The resulting comprehensive maps establish the spatial distribution of potential hydrothermal vents and associated bacteria within a vent field.

Plain Language Summary Detection of diffuse hydrothermal venting is complex as associated fluid density anomalies cannot be detected centimeters above the seafloor. Using a remotely operated vehicle-mounted structured light laser sensor which images a projected laser line at the seafloor, we have demonstrated that remote and systematic detection is possible. The index of refraction and turbulent flow associated with hydrothermal flow distorts the laser line. Detection of this anomaly allows for comprehensive spatial maps of hydrothermal vent fields which can be used to inform geological research objectives and improve ocean exploration.

1. Introduction

Diffuse hydrothermal venting is located within diverse seafloor environments which make automated detection routines complex and inefficient. Low temperature and low flux fluid flow may be found alongside larger point source vents, surrounded by biological activity including bacteria, mussels, clams, and tubeworms, or it can emerge from isolated fissures in the seafloor. The presented approach systematically and efficiently identifies diffuse hydrothermal seafloor venting within varying environments using a structured light laser sensor mounted on a remotely operated vehicle (ROV). The resulting maps place vent field features, including active fluid flow, in a spatial context. This tool will improve the geological understanding of the area, allow for better informed, efficient sampling and near bottom exploration efforts, and aid in documenting temporal changes.

1.1. Geologic Motivation

Low temperature diffuse hydrothermal flow which can occur near low lying mounds and fissures, mixes quickly, and is therefore elusive. The large spatial extent of diffuse flow, in comparison to discrete smokers, allows it to potentially be more influential on chemical and thermal processes of the entire ocean [*Schultz et al.*, 1992]. Currently, there are approximately 689 known sites of hydrothermal activity worldwide [*Beaulieu*, 2015; *Hannington et al.*, 2005]; however, through a combination of vent site observations and heat flux estimates, it is estimated that 90% of fluid flow on mid-ocean ridges is diffuse [*Hannington et al.*, 2011]. Due to detection difficulty, it is likely that the majority of diffuse flow sites have not yet been located or quantified as entire vent fields composed of low flux diffuse flow may remain undiscovered [*Corliss et al.*, 1979; *Baker and German*, 2004]. Accurate distribution of diffuse seafloor venting cannot be established without a near bottom detection method capable of systematically surveying areas greater than a square kilometer in size.

1.2. Review of Existing Vent Detection Methods

Detectable temperature and chemical signals associated with diffuse venting decay within tens of meters of the seafloor due to mixing. In most cases, diffuse vent sites are discovered as a secondary consideration following the localization and exploration of larger point source vents [*German et al.*, 2008] or areas of bacterial mats and biological activity, which rely on vent fluids for survival [*Singh et al.*, 1999; *Shank et al.*, 2003]. For these reasons, the full extent and distribution of diffuse vent fields is rarely determined. Specific approaches for detection of hydrothermal venting have been developed using both visual and acoustic methods.

1.2.1. Point Source Vent Detection

The most successful vent detection schemes focus on point source vents which create buoyant plumes and require various sensors to detect anomalies in magnetics, chemistry or temperature 50–400 m above the seafloor [*Baker and German*, 2004]. Following the detection of a potential plume, vehicle surveys with higher spatial resolution help to distinguish the location of the vent source [*German et al.*, 2008]. It is not until during more targeted dives that detailed optical, acoustic, or tactile investigations of the vent field can be completed [*Singh et al.*, 1999]. At known vent sites three-dimensional acoustic maps of active smokers have provided volumetric flow analysis and heat flux estimates [e.g., *Light et al.*, 2012; *Bemis et al.*, 2015; *Rona et al.*, 2015; *Xu et al.*, 2013].

1.2.2. Diffuse Vent Detection

Traditionally, diffuse flow is detected visually by watching ROV video feeds for "shimmering water," which is generally the only visible indicator [*Bell et al.*, 2012]. The shimmer, or mirage effect, is caused by the presence of fluids with altered indices of refraction due to differences in water temperature, salinity, and chemical composition [*Millard and Seaver*, 1990]. Experiments recreating this visual anomaly in lab settings produce Schlieren-like flows which highlight the density fluctuations. With sufficiently defined parameters a quantitative description of a particular flow and the index of refraction can be made [*Richard and Raffel*, 2001; *Dalziel et al.*, 2000]. Searching for shimmering water with the human eye is time consuming and unsystematic, as this phenomena can be only visible within tens of centimeters of the seafloor; however, it is the most common way to determine areas of scientific interest.

Acoustic approaches for identifying and tracking diffuse flow have included detecting uncorrelated acoustic backscatter caused by temperature-dependent changes in acoustic impedance. Early efforts are detailed in *Rona et al.* [1997] including scanning a 330 kHz Mesotech conical beam sonar parallel to the seafloor to intercept rising near bottom diffuse flow. During data collection the sonar remained stationary and was positioned to minimize seafloor obstructions. Advancements to this acoustic scintillation method allow the sonar to be mounted on an ROV; however, as the sonar must remain stationary during the survey a hovering, stop and start approach was executed [*Rona et al.*, 2002]. Similar technology is implemented on the Cabled Observatory Vent Imaging Sonar (COVIS), a stationary structure with adjustable sonar systems designed to image hydrothermal activity within the Main Endeavour Field, Juan de Fuca Ridge [*Bemis et al.*, 2015].

2. Structured Light Laser Sensor

Initially developed for subcentimeter bathymetric mapping [*Roman et al.*, 2010], the structured light laser system images a projected laser sheet as it is incident with the seafloor, showing the surface topography as if it were sliced along the laser plane. Using triangulation and an accurate laser calibration, the vertical position of the laser line within each image can be converted to a bathymetric profile, analogous to a single ping of range data from a multibeam sonar [*Inglis et al.*, 2012; *Bruno et al.*, 2011; *Moore and Jaffe*, 2002; *Moore et al.*, 2000; *Tetlow and Spours*, 1999].

The structured light laser sensor is a component of the high-resolution mapping suite mounted on the ROV *Hercules* (Figure 1) which also includes stereo cameras. This system has been used to collect coregistered subcentimeter mapping data at geological, archeological, and biological sites [*Roman et al.*, 2012]. The 6000 m rated structured light laser system consists of a 12-bit mono Prosilica camera with a 30° × 40° field of view in water and a verged 100 mW 532 nm green sheet laser manufactured by Coherent PowerLine. The laser and camera are mounted to a rigid frame with known relative geometry.

2.1. Survey Methodology

During a high-resolution imaging survey the vehicle is flown with a constant heading at velocities between 15 and 25 cm/s, and at a constant altitude between 2 and 4 m above the seafloor. The laser line is imaged at approximately 20 Hz, creating a nominal survey resolution of one laser line per centimeter along track and

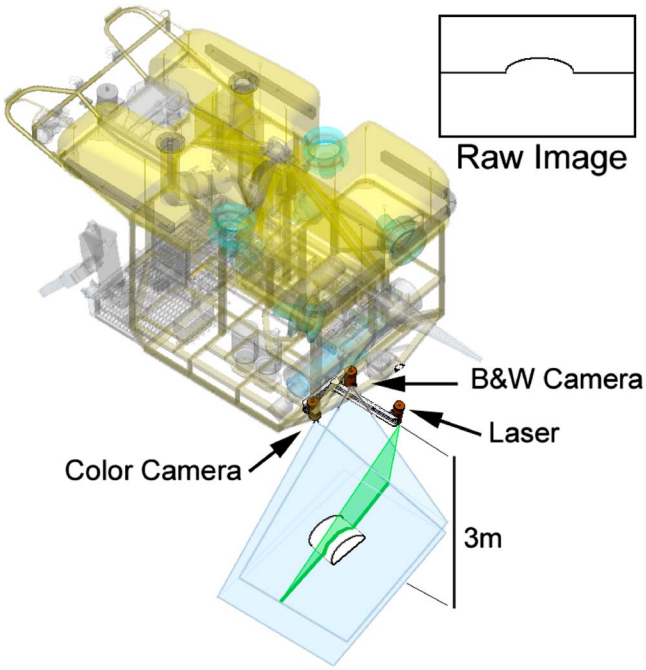

Figure 1. A computer rendering of ROV *Hercules* showing the stereo camera pair and structured light laser sensor mounted on the back of the vehicle away from operational lights. The projected sheet laser is imaged at the seafloor (inset).

2–4 laser points (pixels) per centimeter across track. The range resolution is dictated by the camera and laser geometry, and is approximately 0.5 cm per camera pixel. Strobe lit stereo images with the same 30° × 40° field of view are acquired at 0.33 Hz, interlaced with the laser frames. Trackline spacing is set such that across track overlap between is at least 20%. A survey 30×30 m in size can be completed in about 45 min and the collected data can be gridded to centimeter resolution.

Mounting the imaging system at the back of the vehicle, away from the ROV's forward operational lights improves the signal-to-noise ratio of the images. This ROV is closed loop controlled and capable of executing prescribed tracklines at a constant velocity, altitude, or depth. The navigation sensors include a 600 kHz Teledyne RDI Doppler Velocity Log (DVL), IXSEA OCTANS fiber-optic gyroscope and a Paroscientific depth sensor [*Bell et al.*, 2016]. These data are collected using the DVLNAV software package [*Kinsey and Whitcomb*, 2004].

2.2. Vent Detection With a Structured Light Sensor

Diffraction of the laser line occurs as the structured light laser sensor passes over active venting. Image processing algorithms implemented to detect this anomaly as a proxy for active diffuse hydrothermal venting were presented in *Smart et al.* [2013]. Limitations of this initial work included false positive indications of active venting in the presence of biology, sensitivity to seafloor bathymetry, and poor robustness over varied background and seafloor. This paper will present normalization and classification algorithms to address these limitations.

2.2.1. Interaction With Density Anomalies

In the presence of active hydrothermal fluids the refractive anomaly causes the laser line to appear blurred instead of crisp within the captured mono image (Figure 2a). The increased temperature, salinity, and changing chemical composition of venting fluids alters the ray path. Optical changes are well understood for temperatures up to 30°C and salinity values up to 40 practical salinity units [*Millard and Seaver*, 1990] and are less well defined through interpolation of lab results up to 500°C [*Thormahlen et al.*, 1985]. The turbulent nature of actively venting fluids also creates inhomogeneities causing the index of refraction to vary both spatially and temporally causing continuous angular deviation of the light rays [*Mobley*, 1994] increasing the apparent width of the laser line by 3–8 pixels.

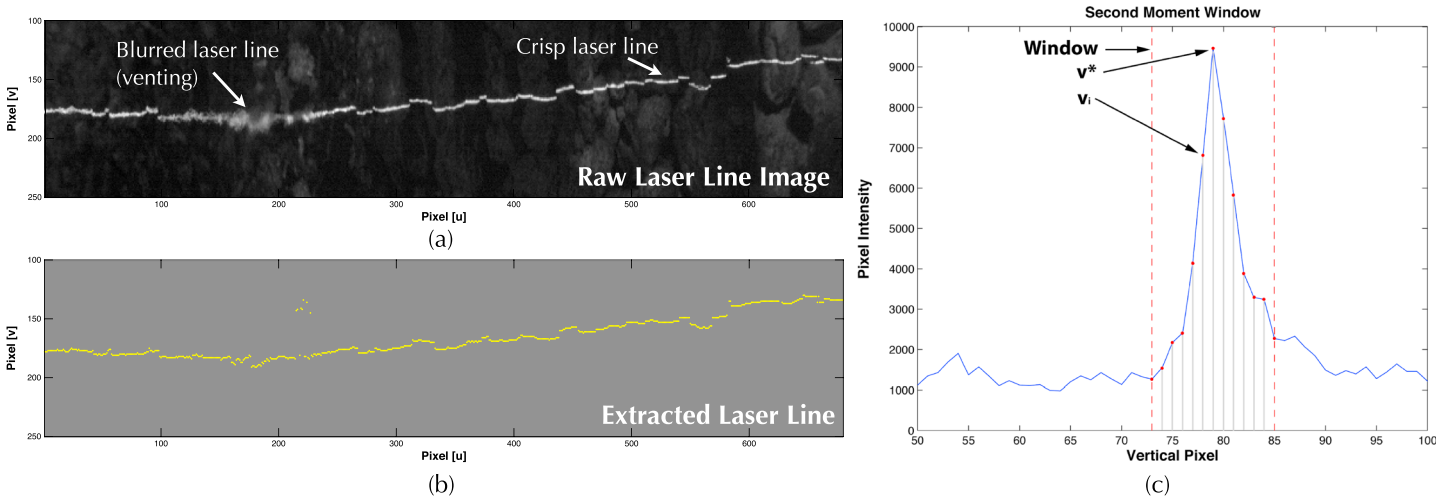

Figure 2. Laser line extraction and processing. (a) In the presence of active venting the laser line is no longer crisp (pixel columns 300–680) instead it appears blurred (columns 200–250). (b) The peak intensity value of the laser line within each image column, recorded as v^*. (c) Cross section of the laser line annotated to define the variables considered for computation of the intensity-weighted second moment about v^* (equation (1)).

To quantify this spread, which serves as a proxy for active venting, the unitless intensity-weighted second moment about the peak intensity value of the laser line, v^*, can be computed by

$$\sum_{i=v^*-\frac{w}{2}}^{v^*+\frac{w}{2}} r_i \left(v_i - v^*\right)^2, \tag{1}$$

where v_i and r_i are the comparison pixel location and intensity respectively and w is the size of the window about the laser line peak. Figure 2c shows a cross section of the laser line identifying these parameters.

2.3. Acquisition and Processing

The image acquisition process (section 2.1) and the subsequent detection and processing of the laser line is largely identical for both the presented vent detection methods and structured light bathymetric mapping [*Inglis et al.*, 2012]. Raw 12-bit black and white images of the laser line incident with the seafloor are thresholded using Otsu's method [*Otsu*, 1979], and image processing algorithms determine the laser line location. The laser extraction batch processing algorithm produces a complete set of profiles and is further detailed in [*Inglis et al.*, 2012; *Smart et al.*, 2013]. With the peak of each laser line cross section, v^*, identified the second moment can be computed using equation (1).

2.4. Creating Maps

Combining the extracted laser data with the corresponding vehicle navigation data produces high-resolution bathymetric, intensity (optical backscatter), and now, seafloor classification maps. No additional acquisition steps are required. The bathymetric data are derived from the location of v^*, which is proportional to range along the laser plane. The normalized intensity values corresponding to v^* indicate variations in seafloor albedo. The structured light laser data can also be coregistered with the stereo imagery and 2-D mosaics. The precision of the coregistration is influenced by the accuracy of the laser calibration routine which is an active area of research.

3. Advancements to Laser Vent Detection

Preliminary diffuse vent detection approaches using the laser rely solely on the intensity-weighted second moment (equation (1)). While the method identified areas of fluid density anomalies, it was also prone to false positives, caused by high second moment values associated with range-dependent laser line intensity and variability of the background seafloor. Errors commonly occurred as the laser passed over reflective seafloor features including bacteria, shells, tubeworms, and man-made objects as addressed in *Smart et al.* [2013]. To correct for these shortfalls, three types of intensity normalization are implemented (section 3.1) and a machine learning approach is taken to classify seafloor characteristics (section 3.2).

3.1. Normalization

Intensity values dominate the weighted second moment computation; therefore, normalization of laser line intensity prior to this computation is important for accurately detecting venting fluid.

3.1.1. Exposure Compensation

During the acquisition process the camera exposure settings are manually adjusted such that the laser line, the signal of interest, appears crisp and bright while the background is predominantly black, resulting in a high signal-to-noise ratio. To account for vehicle lighting, survey parameters and environmental characteristics these settings vary, effectively limiting direct comparison between data collected over multiple surveys without exposure compensation.

Adjusting the intensity range for each survey such that the background pixels are predominately black will establish an intensity baseline. As 99% of the pixels are background data, the mean intensity of an image is a good representation of the minimum intensity, which should be set to zero, or black. Therefore, subtracting this average exposure normalization value from the collected intensity data before laser line extraction, which is not impacted, establishes an intensity baseline for all collected images. To account for lighting changes during the course of a survey, the exposure normalization value is established by computing the mean of 30–50 temporally spaced laser line captures. This normalization process allows for surveys to be directly compared within the same classification routine regardless of site, acquisition date, and exposure settings.

3.1.2. Accounting for Range

Variations in local bathymetry which alter the distance between the camera and seafloor influence the apparent brightness of the laser line. While range variations on the order of a meter would be considered trivial in air, the attenuation of water has a significant impact on intensity [*Mobley*, 1994]. Figure 3 shows a laser line imaged across a plain sloping seafloor in which the seafloor on left side of the image is 2 m from the camera while the seafloor on the right side of the image is nearly 3 m away. The corresponding intensity values and intensity-weighted second moment values are shown on the same horizontal scale to illustrate a noticeably brighter and wider laser line when the camera is closer to the seafloor. This difference can falsely indicate a change in seafloor characteristics and increase the second moment calculation enough to indicate active venting.

Computing the bathymetric range of each point along the laser line allows for normalization using an approach similar to that used in lidar surveys. The intensity value of each laser line point, I_{actual}, is multiplied by the ratio between the recorded range, R_{actual}, and ideal range, R_{expected}, to determine a normalized intensity value, I_{norm} [*Luzum et al.*, 2004]. R_{expected} corresponds to the ROV survey altitude parameter, which is typically 3 m.

$$I_{\text{norm}} = I_{\text{actual}} \times \frac{R_{\text{actual}}}{R_{\text{expected}}} \tag{2}$$

Range normalized intensity and second moment values shown in Figure 3b no longer show range-dependent trends. The resulting laser line intensity values are indicative of changes in seafloor characteristics and not the bathymetry.

3.1.3. Nonuniformity of the Laser Line

Nonuniformity in the brightness along the laser line will also impact the intensity and second moment computations. For example, due to the line generating optical element, the left side of the laser tends to have higher intensity values than the right. Such variations are typical of all laser generators.

The correction approach resembles algorithms for removing lighting artifacts from images taken with external light sources. The along track mean intensity of all thousands of extracted and normalized laser lines is computed effectively averaging away uncorrelated variations in reflectivity. Dividing each normalized extracted laser line by the resulting illumination pattern produces nominally uniform across track illumination.

3.2. Support Vector Machine Implementation

Given the image coordinates, normalized intensity and second moment values for each laser line pixel, a robust multi-class support vector machine (SVM) classification process is implemented to differentiate between plain seafloor, bacteria or other biological activity, and active hydrothermal venting.

A support vector machine (SVM) is a supervised learning method for classification. Labeled training data are used to determine a hyperplane dividing two classes while also maximizing the distance between the

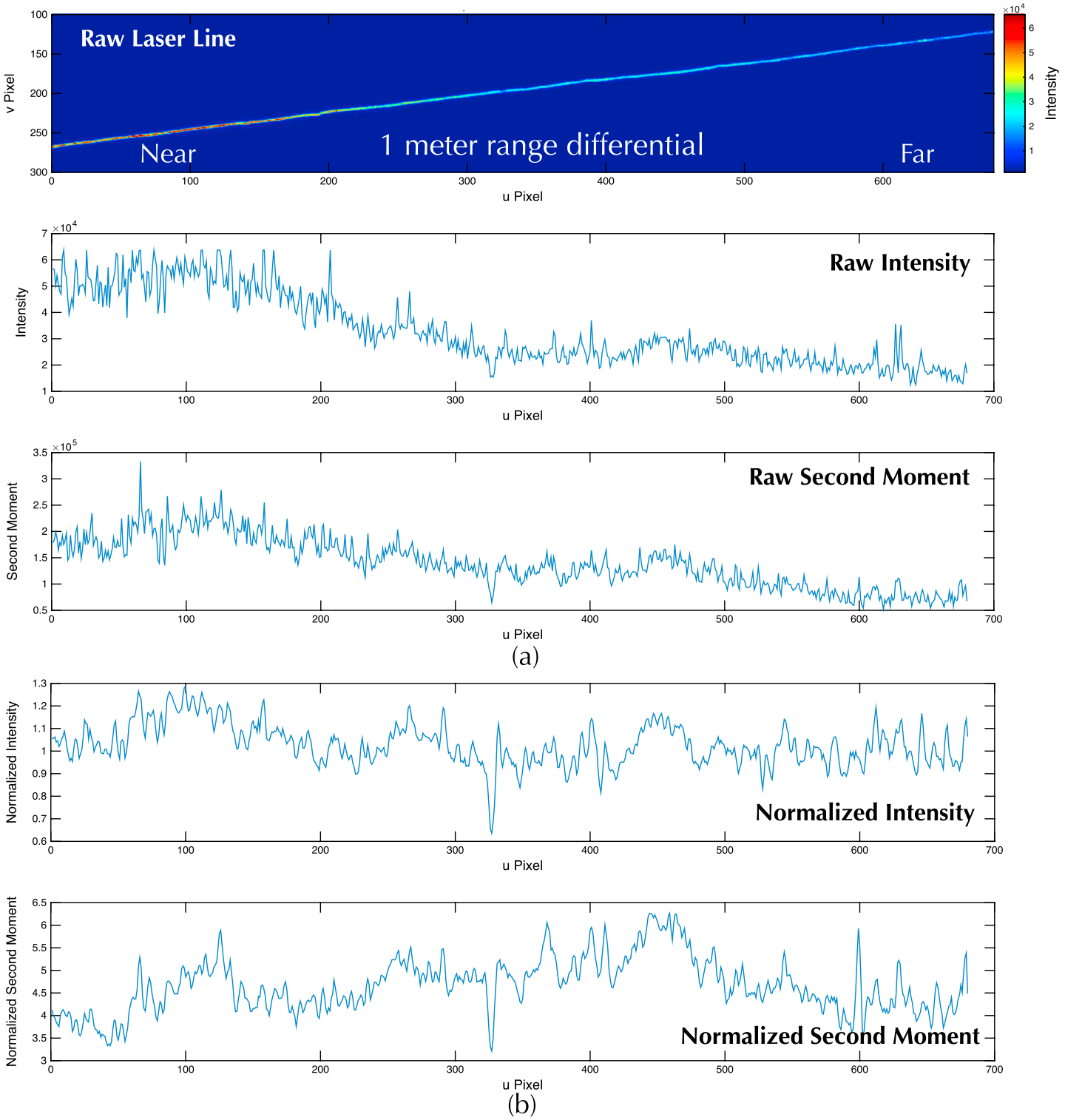

Figure 3. Illustrating the need to account for range, a single laser line imaged while on a slope of plain seafloor where the depth differential across the laser line is approximately 1 m. (a) The left side of the laser line is closer to the camera and the intensity and spread of the laser line are greater, which translates to increased second moment values that affect the vent detection processes. (b) Following range normalization, the resulting intensity and second moment values are more uniform across the image without a bias due to range.

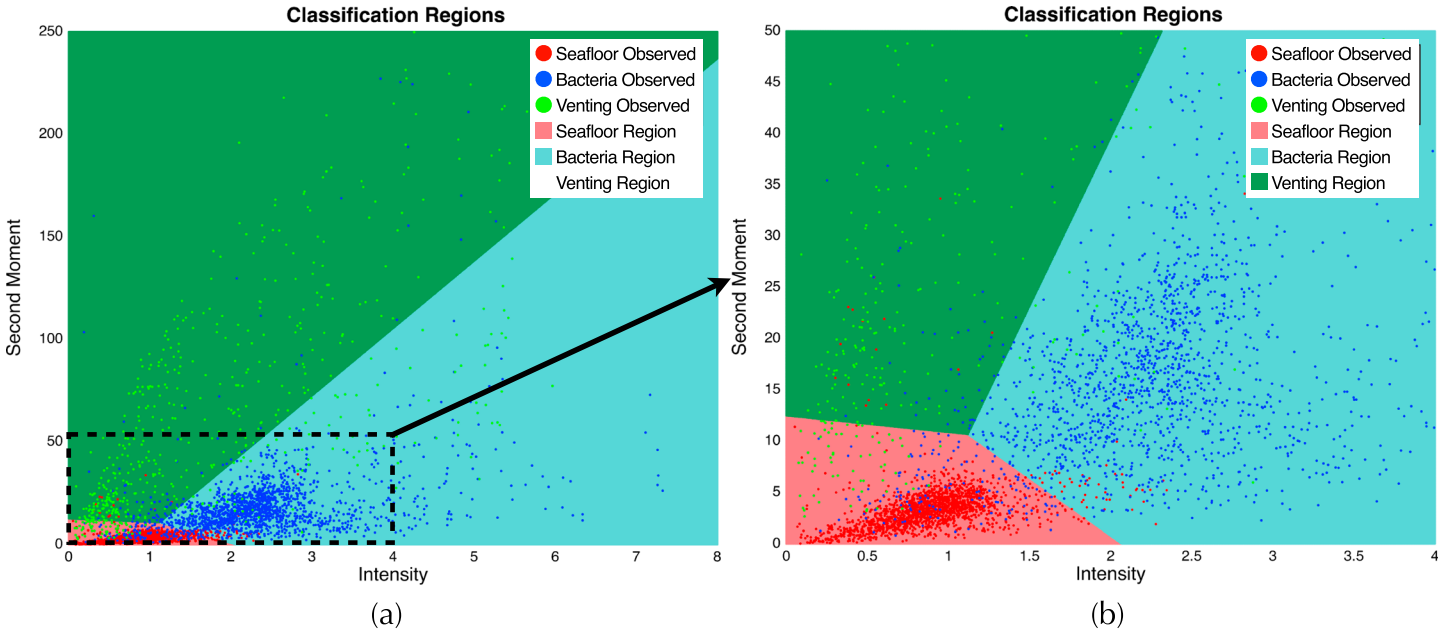

Figure 4. (a) The support vector machine classification space. A point will be classified as seafloor (red area) if both intensity and second moment values are low, bacteria (blue area) if the intensity dominates, and venting (green area) if second moment result is high. The classification training data are plotted as labeled points by color. (b) A zoom in on the transition between the three regions.

hyperplane and data points [*Boser et al.*, 1992]. This nonprobabilistic linear classifier is typically applied to binary data; however, the three class structure of this problem can be decomposed into multiple "one-versus-all" binary classification problems. The output binary classification function with the highest score then determines the class. For instance, a pixel showing *plain seafloor* will receive a high score from the "seafloor versus not seafloor" classifier and low scores from the 'biology versus not biology" and "venting versus not venting" classifiers resulting in a *seafloor* class label. The trained support vector machine will provide boundaries for automatic classification of seafloor, biology, and venting based on feature vectors corresponding to laser line properties.

Training data for this classification routine were hand selected and classified from three different data sets. Compiling a training data set data involved labeling specific pixels after considering the raw laser line images, second moment computation, and laser intensity values in conjunction with high-definition video, stereo imagery, and cruise data. Data collected in 2015 at the Iguanas Vent Field in the Galapagos, Ecuador, which contains three distinct areas of focused flow, diffuse flow, bacteria, and biological activity among pillow basalt yielded approximately 1500 training points. The second set of training data was collected at a cold seep near Kick' em Jenny volcano, Lesser Antilles, which shows an intricate spider web-like pattern of bacteria and biological activity. As no active venting was observed, the 2300 selected points consist of plain seafloor and bacteria, which varied in color and uniformity, resulting in a range of intensity values. The third, and smallest, training data set consisting of 540 training data points, originated from a 2013 survey of a rocky slope with a single active vent on the Mid-Cayman rise. Bacteria is not present at this location, the only observed biological activity was tiny shrimp living at the vent orifice. In total, the complete training set consisted of 4340 hand-selected points with 1930 labeled as seafloor, 1773 representing bacteria, and 637 labeled venting. Further discussion of the training data is presented in section 5.3.

The hand-tagged training data and feature vectors associated with the laser line distribution and intensity were used to develop SVM classifiers. Somewhat unsurprisingly, the features corresponding to the most successful SVM included the intensity of the laser line peak, v^*, and the intensity-weighted second moment. The resulting classifier is shown in Figure 4 with three distinct regions designating plain seafloor (red), bacteria (blue), and venting (green). The training data points are shown in correlating colors. The distribution of this classifier is logical as plain seafloor should have the lowest intensity and minimal laser line spread. The transition between bacteria and venting results from the fact not all light refracted by venting is returned to the camera, and therefore, this class has a lower overall intensity. The presence of bacteria can indicate and

Table 1. Overivew of Support Vector Machine Classification Metrics

	Total	Seafloor	Bacteria	Venting
Full Training Data Set				
Data points	4340	1930	1773	637
Correctly classified	89.8%	96.2%	87.9%	76.0%
Spider Seep				
Data points	2303	1240	1063	0
Correctly classified	96.0%	99.8%	91.4%	0
Cayman Vent				
Data points	541	323	0	218
Correctly classified	81.7%	87.3 %		73.4%
Iguanas Vent				
Data points	1496	367	710	419
Correctly classified	83.4%	91.8%	82.5%	77.3%

obstruct low of active vent fluids, even when not observed by the high-definition (HD) camera, emphasizing the value of classifying bacterial mats. Since training points overlap adjacent classification regions, it is not possible to set decision boundaries with complete classification accuracy; however, as outlined in Table 1, venting was successfully detected with 76% accuracy. These classification metrics outline the percentage of correctly classified points for each data set and indicate robustness of the algorithm to distinguish between plain seafloor and areas of interest within a vent field.

Laser lines collected during a survey over an area with hydrothermal venting are normalized and passed through the SVM classifier. The results can then be presented as waterfall plot of laser lines in time or gridded with navigation to create a geospatial map.

3.3. Spatial and Temporal Averaging to Reduce Noise

The previously described classification process independently analyzes each pixel of the laser line, which captures less than 0.5 cm^2 of seafloor leading to spurious noise within classification results (Figure 5b). Although noise can likely be attributed to hydrothermal particulates in the water and may provide insight into effusion of venting fluids, the resulting classification is cluttered. In an effort to improve classification consistency the intensity results were smoothed both spatially, averaging adjacent pixels of the same laser line (across track), and temporally, considering data from the previous and subsequent laser lines (along track). The intensity-weighted second moment is then computed using these values and passed through the SVM classifier (Figure 5b). The resulting spatially and temporally averaged intensity and second moment images present a distinct vent source within the classification image.

4. Results

Detection of diffuse hydrothermal venting at three sample sites visited between 2011 and 2014 will highlight the presented diffuse seafloor venting algorithm advancements. All data were collected by the high-resolution imaging suite described in section 2.1. A brief overview of each study site will be provided before presenting the classification results, associated video observations, and sampling efforts.

4.1. Kick' em Jenny Diffuse Flow

Laser data collected in 2014 over a small hydrothermal site within the Kick' em Jenny volcano, Grenada, are classified using the SVM and validated with high-definition video footage, survey data, and temperature samples. Within the crater flocculant rust-colored sediment covers the seafloor, bathymetric features include mounds and extinct iron oxide chimneys, white bacterial mats are present, and diffuse flow is found among cracks [*Carey et al.*, 2014]. The sample area includes a vent orifice where isolated focused flow was observed and sampled using the ROV (Figure 6a, inset). The color photomosaic shown in Figure 6a shows no indication of the vent orifice or active fluid flow, illustrating the difficulty in locating diffuse seafloor venting remotely.

The classification of each normalized laser line pixel is displayed within the SVM classification space for this subset of data in Figure 5a. Note the dominance of red seafloor points, while fewer green points represent

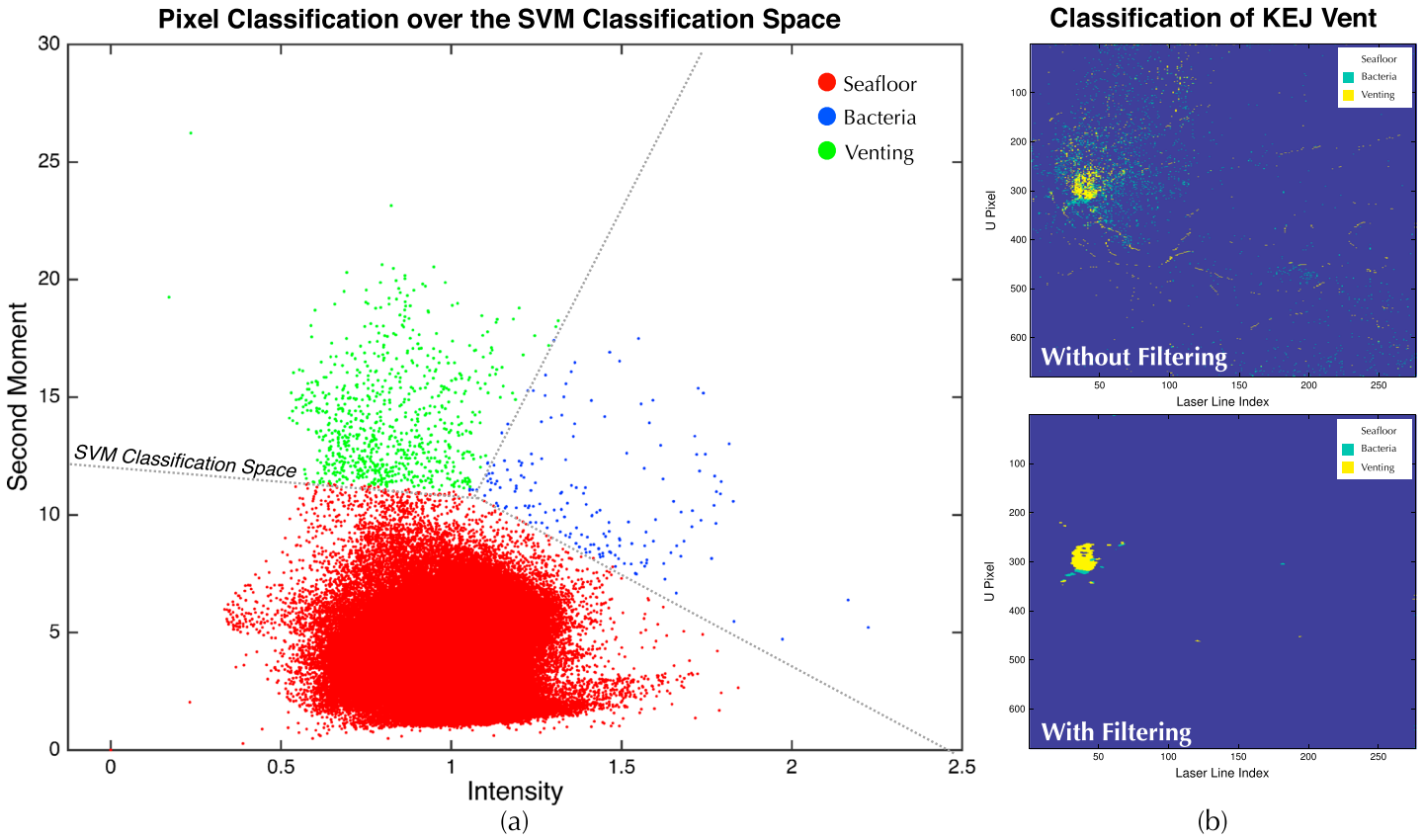

Figure 5. Classification of laser pixels for a subset of data collected at a small point source vent, Kick' em Jenny 2014. (a) Laser pixels plotted within the SVM classification space, classification boundaries are indicated by dotted lines and correspond to Figure 4b. (b) Classified pixels within laser lines. Spurious noise in the classification routine (top) is reduced by spatially and temporally averaging the intensity and second moment results before classification showing a more distinct area of active venting (bottom).

venting and blue points correspond to pixels classified as bacteria. A waterfall of these classified data (276 laser line images each 680 pixels wide) is shown in Figure 5b. This detection result is consistent with the observed focused flow emanating from the vent orifice.

When this data are shown spatially gridded to 1 cm, the area of venting is distinctive (Figure 6b). Within this resulting image blue areas represent seafloor, green is bacteria, and venting is yellow. Although the seafloor is primarily flocculant orange sediment, the detected areas of bacteria have been confirmed, appearing as dark iridescent microbes within the stereo images. Inputs to the classification algorithm include laser intensity which indicates sediment variations (Figure 6c), and the second moment computation which indicates laser line spreads over active fluid flow (Figure 6d).

These detection results align with the observations and sampling during efforts conducted during the ROV dive. The temperature probe recorded an ambient temperature of 13.6°C, a temperature of 21.1°C within the vent orifice, and 19°C above the seafloor within the flow. An additional detected vent site, located approximately 7 m to the south east, consists of diffuse flow emanating from cracks within the seafloor. Temperature probe readings taken at this site recorded 14.1°C as ambient, 86.4°C within the fissure, and 22°C in the diffuse flow.

4.2. Palinuro

Active hydrothermal venting sustains tube worm-dominated biological communities at Palinuro Seamount, Tyrrhenian Sea, Italy. This site was mapped in 2011 and was used in the initial laser vent detection study [*Smart et al.*, 2013]. Differentiation between areas of active fluid flow and areas of dense biological activity as established by the SVM method present more consistent results.

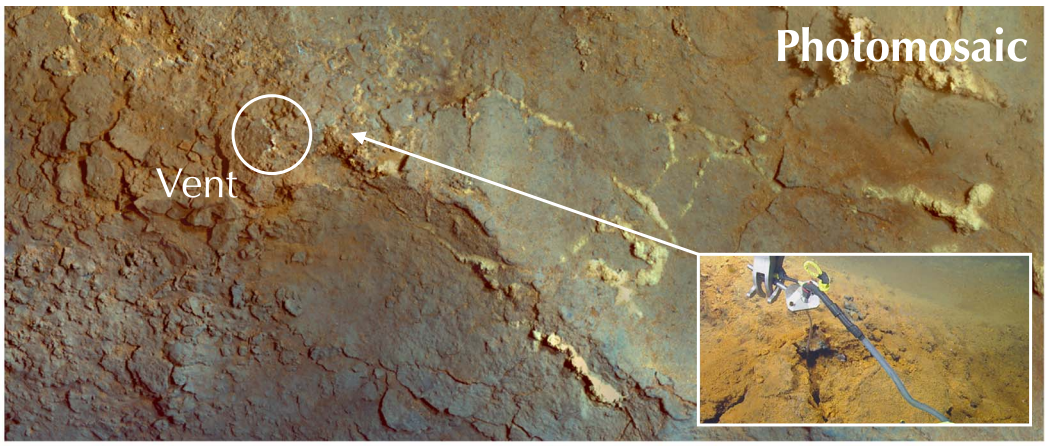

(a)

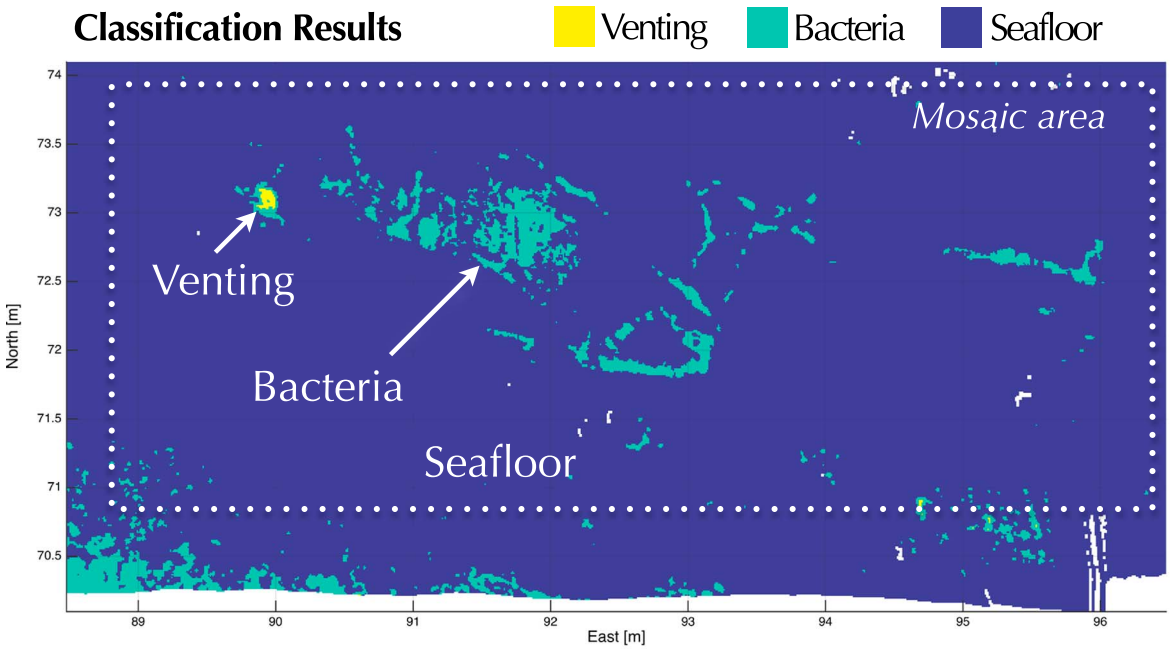

(b)

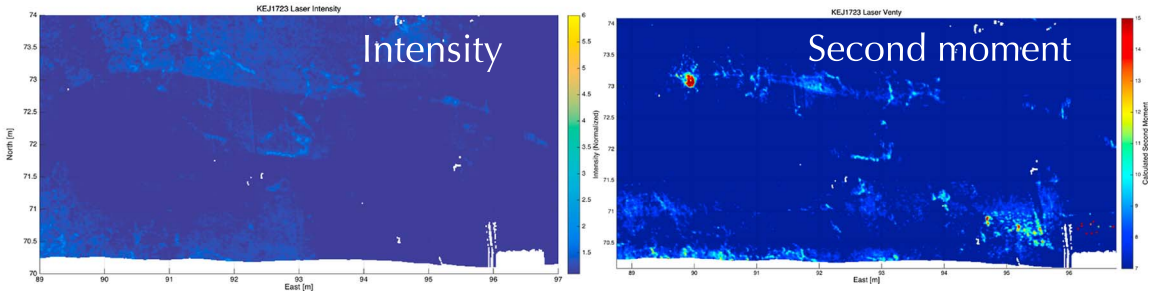

(c) (d)

Figure 6. A survey subset showing the areas of active venting at Kick' em Jenny. (a) Color photomosaic of the area of containing active venting (circle) and HD image of the vent site (inset). (b) Gridded SVM classification result based on intensity and second moment data. (c) Normalized intensity over the site. (d) The second moment computation shows areas of laser line blur.

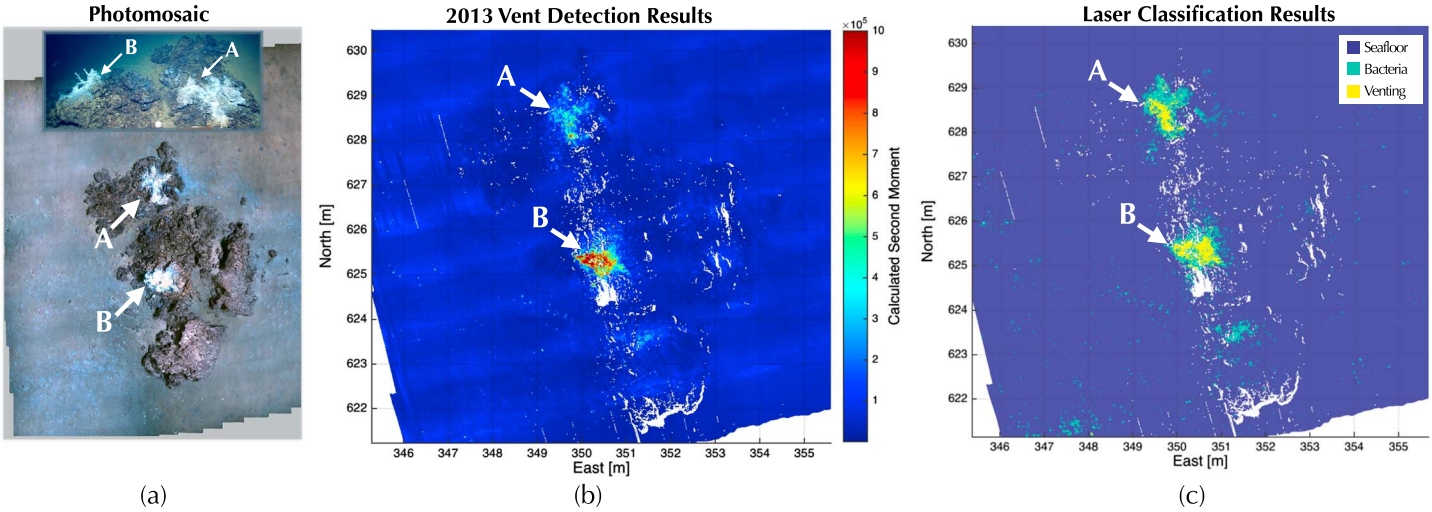

Figure 7. Overview of the Palinuro vent sites. (a) A 2-D photomosaic of the area containing two areas of active venting, labeled A and B, within tube worm colonies living on rocky substrate as seen in the HD capture (inset). (b) Shows the vent detection results using the previous algorithm [*Smart et al.*, 2013] which determined venting based on the un-normalized second moment computation. This image distinctly identifies venting at the southern the tube worm colony, marked B. (c) In comparison, the vent detection using the normalized SVM approach classifies data as seafloor, bacteria, or venting. Distinct areas of active venting appear correctly at both tubeworm colonies, marked A and B.

The primary vent site and the location of tubeworm colonies are shown in the photomosaic and HD image capture (Figure 7a and inset, respectively). This area is relatively flat with two rocky mounds colonized by tubeworms which are surrounded by bacteria. Imagery obtained using the HD video camera observed vigorous flow within both colonies where temperature probe data were collected. Venting at the northern feature had a maximum temperature of 60.4°C, while the southern mound had a maximum temperature of 71.1°C; ambient was 13.5°C.

Highly reflective soft bacteria causes the laser line to bloom due to internal scattering. This effect causes a blurred laser line to be falsely labeled as active venting, instead of bacteria. An example of this is evident when comparing Figures 7b and 7c, where the high intensity bacteria within the southern colony, marked B, dominates the vent detection algorithm. The SVM classification routine independently considers the intensity and computed second moment values. This allows for differentiation between the increased intensity values associated with bacteria and tube worms, and the effects of fluid anomalies. The gridded SVM classification result for this site (Figure 7c) indicates distinct fluid activity surrounded by bacteria on both mounds, which correlates with the results from the visual survey. The result suggests the SVM classification technique is robust to seafloor characteristics and is able to isolate diffuse flow independent of biological activity.

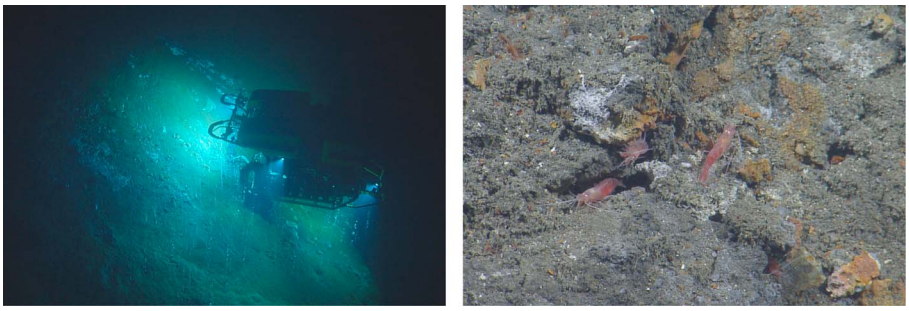

Figure 8. Images providing an overview of Shrimp Vent including bathymetric and biologic activity. (a) HD capture from ROV *Argus* showing *Hercules* working at the shrimp vent site along the south west side of the Kick' em Jenny crater. (b) Shrimp living under rocks and within cracks near the vent fluids.

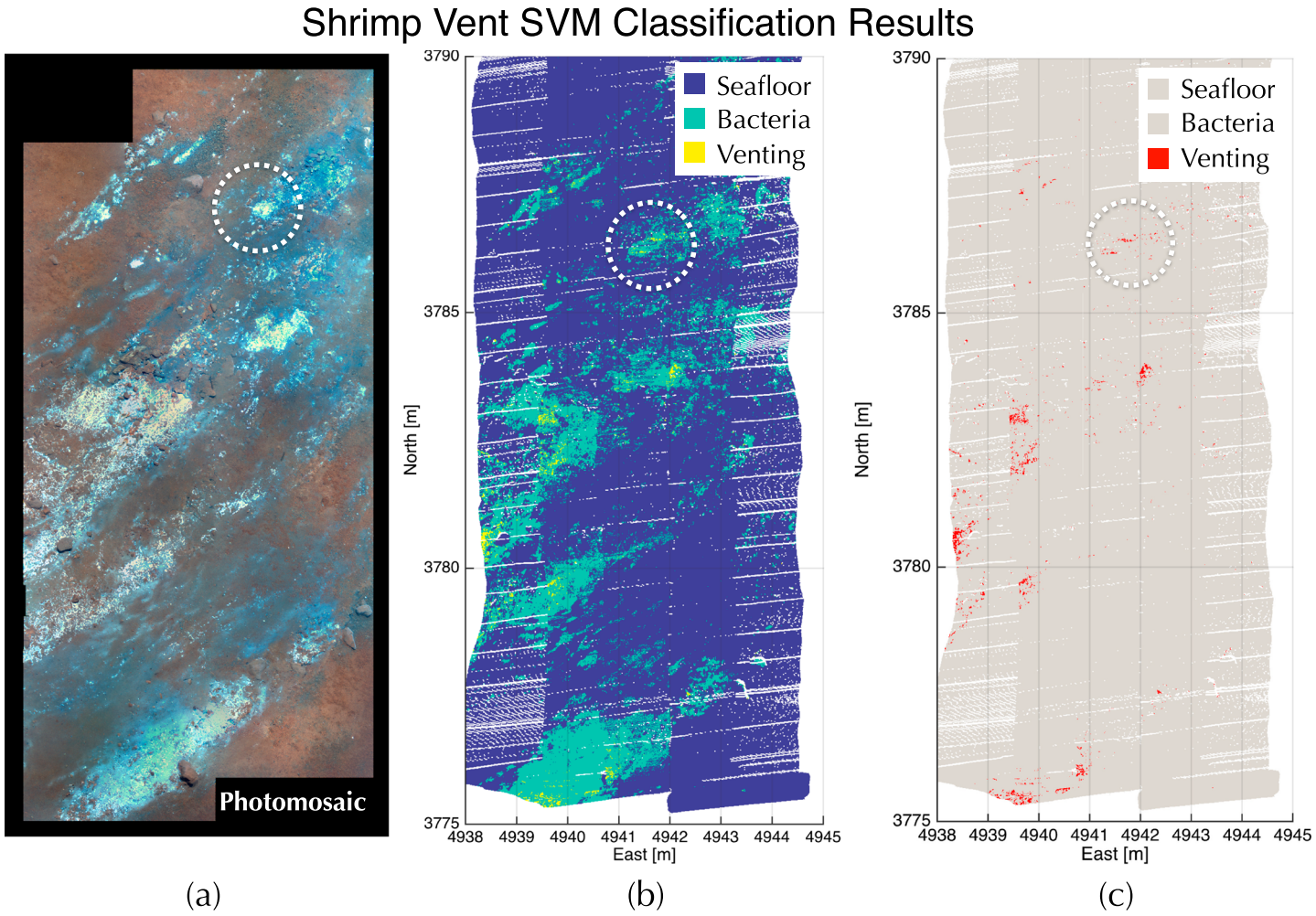

Figure 9. Results of the updated classification algorithm at Shrimp Vent with the main area of sampling indicated by the dashed white circle. (a) 2D photomosaic of the Shrimp Vent area showing the distribution of bacterial mats and seafloor characteristics. (b) Gridded results of the SVM classification method showing seafloor (blue), bacteria (green) and active venting (yellow). (c) Classification algorithm results showing only areas of active venting in red indicating the spatial distribution of active venting.

4.3. Shrimp Vent

The Shrimp Vent area contains prominent areas of venting within the active Kick' em Jenny Crater, Grenada, which E/V *Nautilus* visited in 2013 and 2014. Areas of diffuse fluid flow, and bubbling seeps, are situated on a steep hillside alongside large areas of bacteria and shrimp (Figure 8).

Low flux diffuse venting was prevalent and usually located when closely examining the shrimp. Extensive imaging and physical sampling included biological, water, and temperature samples were collected at the location depicted by the white dashed circle in Figure 9 which corresponds ROV activity in Figure 8a. The maximum recorded temperature was 113.9°C, while nearby flow registered closer to 35°C, and ambient was 14.8°C.

A 90 m^2 subset of the full Kick' em Jenny Crater survey containing the majority of the active Shrimp Vent area is presented in Figure 9. This area represents steep bathymetry with a nearly 10 m differential along the 15 m north-south survey extent as well as the steep western edge of the crater, apparent in Figure 8a. The two-dimensional photo mosaic (Figure 9a) shows extensive bacterial mat coverage. Successfully detecting active venting in an area with these bathymetric and seafloor characteristics is complex and can lead to false positives.

However, bathymetric bias is largely eliminated after implementing the previously discussed range and exposure normalization algorithms. Bacteria is also differentiated from active venting by the SVM classification

algorithm. Gridded classification results shown in Figure 9b indicate areas of bacteria surrounding multiple small areas of diffuse flow. Comparison between the mosaic and this classification result illustrates successful differentiation between seafloor (blue) and bacteria (green), independent of terrain and image acquisition settings. The spatial distribution of small areas of diffuse flow is apparent when viewing only the areas of determined to be part of the active vent class (Figure 9c). The lack of coherence within these areas indicates low rate diffuse flow, likely seeping around rocks and through cracks, as opposed to point source venting.

5. Discussion

5.1. Scientific Benefits and Implications

Systematic remote detection of diffuse seafloor venting will increase comprehensive understanding of the distribution of low flux hydrothermal flow and improve estimates for thermal and chemical ocean budget computations. Additionally, the ability to detect bacteria and associated biological communities which thrive in the presence of hydrothermal or cold seep activity holds additional scientific merit.

5.2. High-Resolution Mapping

5.2.1. Map Creation

The laser line classification results can be viewed in two ways, geospatially or temporally. Detailed analysis of each laser line pixel is possible when data are viewed temporally, as waterfall image (Figure 5b). Although navigation data are unaccounted for, the laser line image index can be cross referenced with vehicle time, navigation, sampling data, and stereo images for vent confirmation

Accurate geospatial maps created by combining laser and navigation data require down sampling the laser data through averaging as data are collected with a density of 3–5 pixels per centimeter across track and 1–2 pixels per centimeter along track. Although this approach creates a smoother map, fills holes, averages outliers, and masks discontinuities, areas of vent activity smaller than 20 cm^2 represented by very few pixels may be lost to averaging. Therefore, vent sites discussed in this paper were gridded on a fine scale to increase the depiction of vent detection at the expense of a cluttered looking map.

Furthermore, impacts of navigation error within a survey were minimized while identifying areas of interest by incorporating ground truth data. Navigation sensors on ROV *Hercules* include a DVL and a ultrashort baseline (USBL) transponder system. The DVL navigation can accumulate error resulting in navigation drift, causing misalignment over large surveys [*Whitcomb et al.*, 1999]. The acoustic USBL system operates between the ship and the vehicle on the seafloor and becomes less accurate in the presence of unknown density stratification due to mixing and while the vehicle is operating near a vertical surface, like a crater wall. Both these scenarios were present while working within the Kick' em Jenny volcano crater, resulting in USBL navigation errors up to 10 m. Ground truth data including images of ROV *Hercules* and key geologic features captured by ROV *Argus*'s HD camera, bathymetric maps, and 2-D mosaics were critical in determining the sample and vent locations. Currently, feature matching is done manually in post processing; however, advancements in structured light mapping efforts will include minimizing navigation error by implementing simultaneous localization and mapping techniques which rely on physical features to constrain navigation [*Roman and Singh*, 2007; *Inglis et al.*, 2012].

5.2.2. Structured Light Laser Calibration

Calibration of the structured light laser system impacts range normalization, the quality of gridded data, and automated registration between imaging data products. This calibration processes is complex and an active area of research [*Inglis et al.*, 2012]. The intensity range normalization requires an accurate calibration to establish the distance between the camera and seafloor. Range errors due to calibration are typically on the order of centimeters and can vary between field seasons if the system is re-calibrated or modified. Within gridded data, calibration error is most noticeable as bathymetric discontinuities between adjacent survey lines and becomes more apparent when data are gridded on a fine scale. Future objectives including automatic correlation of laser pixels and stereo images, and integration of texture and color data into the classification algorithm require a precise laser calibration.

5.3. SVM Classification Algorithm

5.3.1. Training Data and Site Specific SVM Development

The presented SVM classifier was developed using data from three distinct vent sites and has been tested at multiple vent fields with a range of environmental and fluid characteristics. Seafloor training data included

samples of flocculant sediment, hard substrate, rocky outcrops, and pillow basalt. The SVM seafloor classification space effectively determines the sensitivity of the classifier as it defines the lower bounds of the intensity and second moment values for bacteria and vent classification. Therefore, without a prioi knowledge of the seafloor type within a target vent field, a classifier composed of many types of seafloor data is important.

Similarly, the type of active venting included in the training data set must correspond to the type of venting to be detected. To demonstrate the importance of vent type, a second experimental SVM classifier was trained with seafloor and bacteria data from multiple sites, but only one set of vent data from a relatively high flux, high-temperature point source vent. Hand-tagged data collected at a small low-temperature, focused flow vent on the Mid-Cayman rise were then used as test data for this SVM. Due to the inconsistency between vent types used for training and testing, only 57.8% of the test vent data were correctly classified. Conversely, when classifying the same test data set using the original SVM classifier which included training data from multiple types of vent sites, 73.4% of Cayman test data is classified correctly. The ability of a machine classification algorithm to identify both high and low flux active venting is the dependent on the range of data included in the training data set. When detection, venting with various or unknown characteristics is desired and SVM developed using data collected over various types of venting, like the one presented here, should be implemented.

Given a priori knowledge of the area with potential vent sites, the SVM classifier can be optimized based on the type of seafloor and anticipated venting. In practice, data gathered during small a survey of a site, on the order of 200 m^2, can be used as training data for the local area. Ideally, this sample site would include active venting, seafloor and bacteria; however, if data are lacking, previously gathered training data exhibiting similar characteristics will allow for accurate classification.

Hand-labeling SVM training data require gathering features from well understood surveys with varying seafloor, biological, and venting characteristics. The process of hand-selecting data is prone to error, especially in areas where active flow is surrounded by bacteria. Without direct correlation between ground truth data for each pixel, this error is unavoidable. However, the size and diversity of the training data set will minimize the impact of mislabeled training data. While an ideal training data set would include an equal number of samples from each class, seafloor points are very prevalent, bacteria is less so, and confirmed venting is rare.

5.3.2. Detection Limitations

Turbulence and flux appear to have more effect on successful detection than temperature. For instance, the temperature of the vent successfully detected within Kick' em Jenny (section 4.1) was only 7.5°C above ambient. However, the clearly observable focused flow indicates substantial flow and turbulence. In comparison, flow emanating from a fissure at Shrimp Vent with maximum temperature 99.1°C above ambient and only slightly discernible flow was hardly detected using the presented SVM (Figure 9).

5.3.3. Classification Error

Due to the natural variability of the environments surveyed perfect classification is not possible. Seafloor characteristics define the lower vent detection boundary for laser line spread, which faint diffuse flow and quickly diffusing plumes may not exceed. Additionally, in the presence of active venting the laser light scatters, effectively decreasing the recorded intensity values while increasing the spread of the laser line. Unfortunately, active venting occurring over bacteria may return high intensity values and be classified as bacteria. There is still value in this result as bacteria are typically an indication of active hydrothermal activity.

The presented algorithm successfully detects active diffuse flow within an undisturbed environment. However, external disturbances, such as stirred up sediment and man-made objects, can alter the laser line and be identified as either bacteria or venting. For example, fine sediment stirred up by fish can cause scattering of the laser line effectively increasing the width. This error can be manually identified by checking the associated stereo images for a dust cloud. Man-made objects including reflective metal, trash, and scientific markers are not prevalent enough to be accounted for in the classification process and are generally classified as bacteria due to highly reflective nature.

6. Conclusions

Diffuse hydrothermal venting was successfully detected by applying an SVM classification algorithm to data collected systematically and remotely with a structured light laser system. Intensity normalization of the raw laser data eliminates errors due to exposure settings, nonuniformity of the laser line, and seafloor bathymetry.

The SVM method was developed to classify this normalized data as plain seafloor, biologic activity, or active venting. Successful detection has been established across multiple surveys collected within various environments over multiple years. Ideally, this system will be deployed on an ROV or autonomous underwater vehicle during vent field exploration efforts to provide comprehensive maps of areas of potential venting to better inform scientific observation and sampling efforts.

Acknowledgments
The authors would like to acknowledge support of the Roman Lab at the University of Rhode island and the Ocean Exploration Trust which operates the E/V *Nautilus*. Data collection was completed using ROV *Hercules*, owned and operated by Ocean Exploration Trust. Expedition data, including vehicle sensor data, navigation data, video footage, and HD imagery, are available though Ocean Exploration Trust (http://www.oet.org/data-request). High-resolution survey data, including stereo images and structured light laser captures, are available though Chris Roman, Graduate School of Oceanography, University of Rhode Island (croman2@uri.edu).

References

Baker, E. T., and C. R. German (2004), On the global distribution of hydrothermal vent fields, in *Mid-Ocean Ridges*, edited by C. R. German, J. Lin, and L. M. Parson, pp. 245–266, AGU, Washington, D. C., doi:10.1029/148GM10.

Beaulieu, S. E. (2015), Interridge global database of active submarine hydrothermal vent fields: Prepared for interridge. World Wide Web Electronic Publication.

Bell, K. C., P. Nomikou, S. Carey, E. Stathopoulou, P. Polymenakou, A. Godelitsas, C. Roman, and M. Parks (2012), Continued exploration of the Santorini Volcanic Field and Cretan Basin, Aegean Sea, *Oceanography*, *25*(1), 30–31.

Bell, K. C., M. L. Brennan, J. Flanders, N. Raineault, and K. Wagner (2016), Technology, Exploration Vessel Nautilus, *Oceanography*, *29*(1), 4–9, doi:10.5670/oceanog.2016.supplement.01.

Bemis, K. G., D. Silver, G. Xu, R. Light, D. Jackson, C. Jones, S. Ozer, and L. Liu (2015), The path to COVIS: A review of acoustic imaging of hydrothermal flow regimes, *Deep Sea Res., Part II*, *121*, 159–176, doi:10.1016/j.dsr2.2015.06.002.

Boser, B. E., I. M. Guyon, and V. N. Vapnik (1992), A training algorithm for optimal margin classifiers, in *Proceedings of the 5th Annual Workshop on Computational Learning Theory, COLT '92*, pp. 144–152, ACM Press, Pittsburgh., doi:10.1145/130385.130401.

Bruno, F., G. Bianco, M. Muzzupappa, S. Barone, and A. Razionale (2011), Experimentation of structured light and stereo vision for underwater 3D reconstruction, *ISPRS J. Photogramm. Remote Sens.*, *66*(4), 508–518.

Carey, S., et al. (2014), Cold seeps associated with a submarine debris avalanche deposit at Kick'em Jenny Volcano, Grenada (Lesser Antilles), *Deep Sea Res., Part I*, *93*, 156–160, doi:10.1016/j.dsr.2014.08.002.

Corliss, J. B., et al. (1979), Submarine thermal springs on the Galapagos Rift, *Science*, *203*, 1073–1083.

Dalziel, S. B., G. O. Hughes, and B. R. Sutherland (2000), Whole-field density measurements by 'synthetic schlieren', *Exp. Fluids*, *28*, 322–335.

German, C. R., D. R. Yoerger, M. Jakuba, T. M. Shank, C. H. Langmuir, and K. Nakamura (2008), Hydrothermal exploration with the Autonomous Benthic Explorer, *Deep Sea Res., Part I*, *55*(2), 203–219.

Hannington, M., J. Jamieson, T. Monecke, S. Petersen, and S. Beaulieu (2011), The abundance of seafloor massive sulfide deposits, *Geology*, *39*(12), 1155–1158, doi:10.1130/G32468.

Hannington, M. D., C. D. J. de Ronde, and S. Petersen (2005), Sea-floor tectonics and submarine hydrothermal systems, in *Economic Geology, 100th Anniversary*, pp. 111–141, Society of Economic Geologists, Littleton, Colo.

Inglis, G., C. Smart, J. Vaughn, and C. Roman (2012), A pipeline for structured light bathymetric mapping, in *Proceedings of the 2012 IEEE/RSJ International Conference on Intelligent Robots and Systems*, pp. 4425–4432, IEEE, Algarve, Portugal.

Kinsey, J. C., and L. L. Whitcomb (2004), Preliminary field experience with the DVLNAV integrated navigation system for oceanographic submersibles, *Control Eng. Pract.*, *12*, 1541–1549.

Light, R., V. Miller, P. Rona, and K. Bemis (2012), Acoustic instrumentation for imaging and quantifying hydrothermal flow in the NEPTUNE Canada Regional Cabled Observatory at Main Endeavour Field, PDF.

Luzum, B., M. Starek, and K. C. Slatton (2004), Normalizing ALSM intensities, GEM Center Report No. Rep 2004-07-001, Geosensing Engineering and Mapping (GEM) Civil and Coastal Engineering Department, Univ. of Florida.

Millard, R. C., and G. Seaver (1990), An index of refraction algorithm for seawater over temperature, pressure, salinity, density, and wavelength, *Deep Sea Res., Part A*, *37*(12), 1909–1926.

Mobley, C. D. (1994), *Light and Water Radiative Transfer in Natural Waters*, Academic Press, San Diego, Calif.

Moore, K., and J. Jaffe (2002), Time-evolution of high-resolution topographic measurements of the sea floor using a 3-D laser line scan mapping system, *IEEE J. Oceanic Eng.*, *27*(3), 525–545, doi:10.1109/JOE.2002.1040936.

Moore, K. D., J. S. Jaffe, and B. L. Ochoa (2000), Development of a new underwater bathymetric laser imaging system: L-Bath, *J. Atmos. Oceanic Technol.*, *17*(8), 1106–1117.

Otsu, N. (1979), A threshold selection method from gray-level histograms, *IEEE Trans. Syst. Man Cybern.*, *9*(1), 62–66, doi:10.1109/TSMC.1979.4310076.

Richard, H., and M. Raffel (2001), Principle and applications of the background oriented schlieren (BOS) method, *Meas. Sci. Technol.*, *12*, 1576–1585.

Roman, C., and H. Singh (2007), A Self-consistent bathymetric mapping algorithm, *J. Field Rob.*, *24*(1–2), 23–50, doi:10.1002/rob.20164.

Roman, C., G. Inglis, and J. Rutter (2010), Application of structured light imaging for high resolution mapping of underwater archaeological sites, in *Proceedings of the MTS/IEEE Oceans*, pp. 1–9, IEEE, Sydney, Australia.

Roman, C., G. Inglis, J. I. Vaughn, C. Smart, B. Douillard, and S. Williams (2012), The development of high-resolution seafloor mapping techniques, *Oceanography*, *25*(1), 42–45.

Rona, P., D. R. Jackson, T. Wen, C. Jones, K. Mitsuzawa, K. G. Bemis, and J. G. Dworski (1997), Acoustic mapping of diffuse flow at a seafloor hydrothermal site: Monolith Vent, Juan de Fuca Ridge, *Geophys. Res. Lett.*, *24*(19), 2351–2354.

Rona, P., D. R. Jackson, K. G. Bemis, C. D. Jones, K. Mitsuzawa, D. R. Palmer, and D. Silver (2002), Acoustics advances study of sea floor hydrothermal flow, *Eos Trans. AGU*, *83*(44), 497–502.

Rona, P. A., K. G. Bemis, G. Xu, and K. Mitsuzawa (2015), Estimations of heat transfer from Grotto's North Tower: A NEPTUNE Observatory case study, *Deep Sea Res., Part II*, *121*, 95–111, doi:10.1016/j.dsr2.2015.05.010.

Schultz, A., J. R. Delaney, and R. E. McDuff (1992), On the partitioning of heat flux between diffuse and point source seafloor venting, *J. Geophys. Res.*, *97*(B9), 12,299–12,314.

Shank, T., D. Fornari, D. Yoerger, S. Humphris, and A. Bradley (2003), Deep submergence synergy: Alvin and ABE explore the Galapagos Rift at 86 W, *Eos Trans. AGU*, *84*(41), 425–440.

Singh, H., F. Weyer, J. Howland, A. Duester, D. Yoerger, and A. Bradley (1999), Quantitative stereo imaging from the Autonomous Benthic Explorer (ABE), in *OCEANS '99 MTS/IEEE. Riding the Crest into the 21st Century*, vol. 1, pp. 52–57, IEEE, Seattle, Wash., doi:10.1109/OCEANS.1999.799706.

Smart, C., and C. Roman (2017), Detection of diffuse seafloor venting using a structured light laser sensor: 2. Evaluation of detection sensitivity and limitations, *Earth and Space Science*, *4*, doi:10.1002/2017EA000263.

Smart, C. J., C. Roman, and S. N. Carey (2013), Detection of diffuse seafloor venting using structured light imaging, *Geochem. Geophys. Geosyst.*, *14*(11), 4743–4757, doi:10.1002/ggge.20280.

Tetlow, S., and J. Spours (1999), Three-dimensional measurement of underwater work sites using structured laser light, *Meas. Sci. Technol.*, *10*(12), 1162–1167.

Thormahlen, I., J. Straub, and U. Grigull (1985), Refractive index of water and its dependence on wavelength, temperature and density, *J. Phys. Chem.*, *14*, 933–945.

Whitcomb, L., D. Yoerger, and H. Singh (1999), Advances in Doppler-based navigation of underwater robotic vehicles, in *Proceedings 1999 IEEE International Conference on Robotics and Automation (Cat. No.99CH36288C)*, vol. 1, pp. 399–406, IEEE, Detroit, Mich.

Xu, G., D. R. Jackson, K. G. Bemis, and P. A. Rona (2013), Observations of the volume flux of a seafloor hydrothermal plume using an acoustic imaging sonar, *Geochem. Geophys. Geosyst.*, *14*, 2369–2382, doi:10.1002/ggge.20177.